C. R. Physique 15 (2014) 884–897

Contents lists available at ScienceDirect

Comptes Rendus Physique

www.sciencedirect.com

The Sagnac effect: 100 years later / L'effet Sagnac 100 ans après

Large-area Sagnac atom interferometer with robust phase read out

Interféromètre Sagnac atomique avec une acquisition de signal robuste

Gunnar Tackmann *, Peter Berg *, Sven Abend, Christian Schubert, Wolfgang Ertmer, Ernst Maria Rasel

Institut für Quantenoptik, Gottfried Wilhelm Leibniz Universität Hannover, Welfengarten 1, 30167 Hannover, Germany

ARTICLE INFO

Article history:
Available online 18 October 2014

Keywords:
Atom interferometer
Gyroscopes
Inertial sensing
Cold atoms

Mots-clés :
Interféromètre atomique
Gyromètres
Capteurs inertiels
Atomes froids

ABSTRACT

We report on recent progress on our matter-wave Sagnac interferometer capable of resolving ultra-slow rotations below the $\mu\mathrm{rad\,s^{-1}}$ level with a 1-s measurement time and a repetition rate of 2 Hz. Two Raman interferometers are employed that are susceptible to rotation and acceleration. We demonstrate two read-out schemes exploiting the strict phase correlation of the dual interferometer, the first one locking the interferometer to the mid-fringe position, and the second relying on phase modulation combined with ellipse fitting. In both, the sensitivity to gravity acceleration is employed for controlling the differential interferometer phase without influencing the rotation signal. Furthermore, we discuss errors in the rotation signal arising from atom source instabilities combined with a residual misalignment of the three pulsed light gratings used for atomic diffraction. Monitoring the source position fluctuations allows us to suppress this spurious signal. We achieve stable operation with a sensitivity of 850 $\mathrm{nrad\,s^{-1}\,Hz^{-1/2}}$ for a 1-s measurement time, and 20 $\mathrm{nrad\,s^{-1}}$ after 4000 s of averaging.

RÉSUMÉ

Nous présentons ici les progrès réalisés avec notre interféromètre Sagnac à ondes de matière capable de résoudre des rotations ultra-lentes de l'ordre du $\mu\mathrm{rad\,s^{-1}}$ avec un temps de mesure de 1 s et un taux de répétition de 2 Hz. Deux interféromètres Raman, sensibles aux rotations et aux accélérations, ont été utilisés. Nous avons développé deux techniques d'acquisition de signal qui exploitent la corrélation de phase du double interféromètre, la première en stabilisant l'interféromètre sur la position à mi-frange, la deuxième se basant sur la modulation de phase en combinaison avec la méthode dite *ellipse fitting*. Les deux techniques reposent sur la sensibilité à l'accélération gravitationnelle qui est utilisée pour contrôler la phase différentielle sans perturber la phase de rotation. De plus, nous discutons dans cet article des erreurs dans la mesure de la rotation engendrées par des instabilités des sources atomiques croisées, avec un non-alignement résiduel des trois réseaux optiques qui sont utilisés pour la diffraction atomique. L'enregistrement des fluctuations de la position des sources nous permet de réduire ce signal parasite. Nous atteignons ainsi une

* Corresponding authors.
E-mail address: rasel@iqo.uni-hannover.de (E.M. Rasel).

http://dx.doi.org/10.1016/j.crhy.2014.10.001
1631-0705/

sensibilité d'opération stable de 850 nrad s^{-1} Hz$^{-1/2}$ à une seconde de temps de mesure et 20 nrad s^{-1} après 4000 s d'intégration.

1. Introduction

Since the discovery of the rotation-induced phase shift in an interferometer with area-inclining paths, the Sagnac effect [1] has become the basis for high-precision rotation measurements [2]. The first observation of this effect, demonstrated by Georges Sagnac in 1913, was realized with a spectrally refined light field emitted from an electric lamp. Over the last century, the technological advances, in particular the invention of the laser, boosted the sensitivity of light-based Sagnac interferometers. Moreover, the possibility of coherently manipulating neutral atoms with laser light enabled the development of matter-wave-based Sagnac interferometers, subject of this article. In both, light and atom interferometers rotation measurements rely on the Sagnac phase:

$$\Phi_{\text{Sagnac}} = \frac{2E}{\hbar c^2}\boldsymbol{\Omega}\cdot\mathbf{A} \tag{1}$$

where E is the particle energy of the interfering photons or atoms, respectively. Furthermore, $\hbar$ is the reduced Planck constant, c the speed of light, $\boldsymbol{\Omega}$ the rotation, and $\mathbf{A}$ the area enclosed by the interferometer paths. This yields an advantage in the interferometer scaling factor for atoms featuring much higher particle energy. Comparing the energy $E = \hbar\omega$ of photons at the helium–neon laser wavelength of $\lambda_{\text{HeNe}} = 2\pi c\omega^{-1} \approx 633$ nm with the energy of rubidium-87 atoms at low velocities $E = m_{^{87}\text{Rb}}c^2$ yields an increase factor of 1.2×10^{11} in the Sagnac phase for given area and rotation rate. This huge factor is put into perspective by the fact that typical sources for matter-waves have relatively low particle flux leading to high shot-noise [3], and the realization of areas as large as several square centimetres or even many square meters has yet to be demonstrated with matter-waves. Nevertheless, the tremendous boost in the Sagnac scale factor allows the realization of highly compact devices capable of reaching sensitivities comparable with state-of-the-art laser gyroscopes. Furthermore, the absolute value of the area enclosed by a matter-wave Sagnac interferometer is well-controlled through the well-known atomic mass and, in case of atom interferometers involving light gratings for atomic diffraction, the photon-induced atomic recoil velocity, yielding a high accuracy and stability in the rotation measurement.

The most sensitive atom interferometer gyroscopes employ light gratings for atomic beam splitting. Atom interferometers based on this technique have rapidly evolved to high-precision tools for measurements of fundamental physical constants [4–7], electromagnetic fields [8], and inertial forces [9] within the last two decades. The cornerstone for these interferometers is the coherent manipulation of the internal and external atomic degrees of freedom using laser light. Precision gyroscopes based on this concept have been pioneered by groups at Stanford University and at SYRTE ("Systèmes de référence temps espaces") in Paris. The work in Stanford led to the first development of a dual atom interferometer gyroscope [10] using two thermal beams of neutral cesium atoms. It reached sensitivities of down to 0.6 nrad s^{-1} Hz$^{-1/2}$ inferred from the instrument's signal-to-noise ratio [11], only one order of magnitude less than today's best ring–laser gyroscopes [12]. The group at SYRTE realized a dual atom interferometer capable of measuring all six axes of inertia using two laser-cooled atomic clouds counter-propagating on superimposed trajectories and a single-light grating that was pulsed in time [9]. These works yielded a much more compact and highly sensitive cold-atom gyroscope with a demonstrated sensitivity of 240 nrad s^{-1} Hz$^{-1/2}$ and 10 nrad s^{-1} after integration [13].

In this article, we present advances on our atomic dual Sagnac interferometer, which uses three spatially separated light gratings that are pulsed in time for splitting, redirecting, and recombining the interferometer paths enabling large interferometer areas and therefore high rotation sensitivity. We present two different robust rotation signal read out techniques exploiting the correlation of the two interferometers. The use of three single light gratings sets high demands on the relative alignment of the employed laser beams as well as on the control of the atomic sources position and launch velocities. These demands and their impact on the gyroscope measurement stability are discussed in detail in this article, which is organized as follows: Section 2 describes the operation principle of Raman light-pulse atom interferometers and, in particular, of our atomic gyroscope. In Section 3, the gyroscope measurement procedure and technical setup are described. Section 4 introduces the obtained interferometer signals and derives the sensitivity of a rotation measurement using the dual Raman interferometer. The robust read-out techniques are introduced in Section 5, and the long-term stability of the rotation measurement as well as the major source for slow fluctuations are discussed in Section 6, before concluding on the achieved results in Section 7.

2. Measuring rotation with atom interferometry

The functional principle of our light-pulse–atom-interferometer-based inertial sensor relies on matter-wave diffraction on light gratings formed by counter-propagating laser beams transferring two photon momenta to the atoms [14,15]. The thereby induced Rabi oscillations occurring between different atomic momentum states enable the realization of coherent

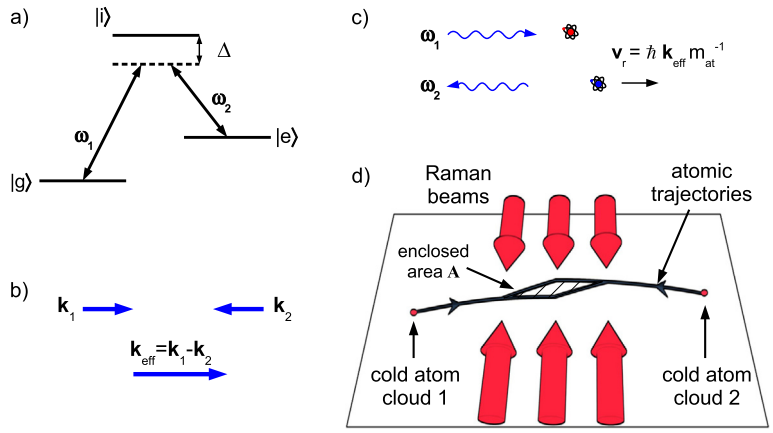

Fig. 1. (Colour online.) Raman atom interferometer. (a) We drive Raman transitions between internal atomic states $|g\rangle$ and $|e\rangle$ by shining in two light fields of frequencies ω_1 and ω_2. Each light field features a large detuning Δ with respect to an intermediate atomic state $|i\rangle$, so that single-photon transition rates are negligible. (b) By shining in the light fields from opposite sides, we realize an effective wave vector $\mathbf{k}_{\text{eff}}$, which defines the momentum $\hbar\,\mathbf{k}_{\text{eff}}$ transferred to the atoms. (c) An atom undergoing the stimulated Raman transition gains a velocity component $\mathbf{v}_{\text{r}}$. (d) The dual Sagnac atom interferometer is realized by launching atomic clouds onto parabolic trajectories and interrogating them with three horizontal counter-propagating pairs of Raman laser beams along their free fall. The enclosed area makes the interferometer susceptible to rotations of the device.

atom-optical elements. Depending on the Rabi angle, being the product of Rabi frequency Ω_{Rabi} and pulse duration τ, it is possible to create a coherent superposition of two momentum states, or even to fully transfer the atoms from one momentum state to the other. The assigned light pulses that correspond to beam splitters and mirrors are called $\pi/2$- and π-pulses, respectively. This process implies a resonance condition on the frequency difference of the two counter-propagating laser beams, which is the equivalent to the Bragg angle condition in the well-known case of an electromagnetic wave impinging on a solid-state crystal structure [16]. Choosing the frequency difference of the counter-propagating laser beams equal to this Bragg resonance frequency plus a frequency corresponding to an atomic transition energy difference allows us to drive a stimulated Raman transition, which coherently couples internal and external atomic degrees of freedom. Hence, the atom performs an internal state transition from ground state $|g\rangle$ to excited state $|e\rangle$ if, and only if it acquires a photon recoil momentum of $\hbar k_{\text{eff}}$ corresponding to the effective recoil of the two counter-propagating light fields (see also Fig. 1). This allows us to entangle the internal and external atomic states and thereby to detect the external atomic state population by reading out the internal state population. This has been first introduced by Christian Bordé as state-labelling [17].

An interferometer is formed by applying $\pi/2$- and π-pulses separated by the interferometer free evolution times T during which the atom interferometer paths drift apart from or towards each other when they are in different momentum (and thus also internal) states. While more complex schemes are often used (see, e.g., [9]), we will restrict ourselves to the so-called Mach–Zehnder-like interferometer scheme consisting of one initial beam splitter or $\pi/2$-pulse, a mirror or π-pulse that inverts the momenta of the interferometer arms, and a second $\pi/2$-pulse that closes the interferometer. The two resulting interferometer output state populations oscillate as a function of the interferometer phase. Assuming the preparation of an atomic ensemble in a well-defined momentum state in the internal ground state, the interferometer phase determines the so-called transition probability, which reads:

$$P_{\text{e}} = \frac{1}{2} - \frac{1}{2}\cos(\Phi) \tag{2}$$

This performs a typical interferometer fringe pattern as a function of the total interferometer phase:

$$\Phi = \Phi_{\Omega} + \Phi_{\text{a}} + \Phi_{\text{laser}} + \Phi_{\text{EM}} \tag{3}$$

containing contributions arising from rotations (Φ_{Ω}) and accelerations (Φ_{a}). In addition, the interferometer phase comprises contributions from the relative phase of the two laser light fields (Φ_{laser}) as well as a phase shift from electromagnetic-field induced atomic level shifts (Φ_{EM}).

2.1. Atomic Sagnac interferometer

In order to create a maximal area for a given interferometer pulse separation time T, the beam-splitting direction is chosen to be perpendicular to the atomic forward velocity (see Fig. 1). Taking into account the atomic velocity $\mathbf{v}_{\text{at}}$ and the recoil velocity v_{r} gathered by the atom during the beam-splitting process, the enclosed area depicted in this configuration is found to be $\mathbf{A} = \mathbf{v}_{\text{atom}} \times \mathbf{v}_{\text{r}} T^2$. The recoil velocity $\mathbf{v}_{\text{r}} = \hbar\,\mathbf{k}_{\text{eff}}\, m_{\text{at}}^{-1}$ contains the atomic mass m_{at}, and the two-photon wave vector $\mathbf{k}_{\text{eff}} = \mathbf{k}_1 - \mathbf{k}_2$. With the Sagnac formula (Eq. (1)), this results in a rotation-induced atom interferometer phase of

$$\Phi_{\Omega} = 2(\boldsymbol{\Omega} \times \mathbf{v}_{\text{atom}}) \cdot \mathbf{k}_{\text{eff}}\, T^2 \tag{4}$$

This phase shift can also be derived in a slightly different way: according to [14], the laser grating phase ϕ_i is imprinted on the matter-wave phase during each atom–light interaction i, leading to a total phase shift of

$$\Phi = \phi_1 - 2\phi_2 + \phi_3 \tag{5}$$

Here, each phase term $\phi_i = \phi_i(t) + k_{\text{eff}} d_i$ (applied during the pulses $i = 1, 2, 3$) comprises a temporal and a spatial part, where d_i is the normal distance separating the atom and a well-defined phase–plane position, which is in our case given by the mirror surfaces retro-reflecting the Raman beams (these are introduced in Section 3). This results in an interferometer phase shift in case light-fields are accelerated with respect to the atom in free fall along the interferometer paths. For an effective wave vector of the multi-photon process $\mathbf{k}_{\text{eff}}$ and an acceleration $\mathbf{a}$, this phase shift is found to be first order [14]:

$$\Phi_{\text{a}} = \mathbf{a} \cdot \mathbf{k}_{\text{eff}} T^2 \tag{6}$$

This also allows us to derive the rotation-induced phase shift by considering the Coriolis acceleration $\mathbf{a}_{\text{Coriolis}} = 2(\boldsymbol{\Omega} \times \mathbf{v}_{\text{atom}})$ reproducing Eq. (4). These considerations yield the inertial phase shifts in first order. Higher-order phase shifts as those considered in [18] can be neglected for the parameter range used in our interferometer.

In order to discriminate between phase shifts induced by acceleration and rotation, we employ two interferometers with atoms travelling on parabolic trajectories with opposite horizontal velocities, as depicted in Fig. 1. The signs of the photon momenta transferred to the atoms in the two clouds are opposite, which will be explained in more detail in Section 3. This causes the acceleration phase to flip sign while the rotation phase is common for both interferometers. The phases measured by the two interferometers can therefore be written as:

$$\Phi_1 = \Phi_\Omega + \Phi_{\text{a}} + \Phi_{\text{laser}} + \Phi_{\text{EM},1} \tag{7}$$

$$\Phi_2 = \Phi_\Omega - \Phi_{\text{a}} + \Phi_{\text{laser}} + \Phi_{\text{EM},2} \tag{8}$$

The rejection of the phase shifts induced by electromagnetic fields is then realized in the so-called k-reversal technique, which will be introduced in Section 3.2. The laser-induced phase shift Φ_{laser} enables us to add a phase shift to control the interferometer point of operation, which leaves us with the rotation-induced phase shift Φ_Ω.

3. Experimental realization

The gyroscope apparatus containing the two atom interferometers depicted in Fig. 2 was first described in [19]. Each of the two interferometers is created with atomic clouds of ^{87}Rb that are magneto-optically trapped and launched on a parabolic trajectory [20]. The atomic ensembles are launched with a horizontal velocity of 2.79 $\text{m}\,\text{s}^{-1}$, and a vertical velocity of 0.73 $\text{m}\,\text{s}^{-1}$. On their flight of about 120 ms, the matter-waves are initially prepared in the interferometer ground state, then split, redirected and recombined with a typical interferometer pulse separation of $T = 23$ ms, resulting in an area of $A = 17.4$ mm^2. We employ retro-reflected bi-frequency light fields for Raman beam-splitting that are pulsed in time in three parallel beams in the horizontal plane when the atomic clouds travel almost perpendicularly to the beams' optical axes. The transition probability P_{e} is then measured in a state-selective fluorescence detection at the end of the free fall.

3.1. Interferometer states

The atoms exit the source in clouds with temperatures around 8 μK and particle numbers of 10^8 in the hyperfine state $|5^2S_{1/2}, F = 2\rangle$, spread over all Zeeman sublevels. A first velocity selective Raman π-pulse selects atoms of a well-defined velocity class [21] that are transferred from the excited state $|e\rangle = |5^2S_{1/2}, F = 2, m_F = 0\rangle$ to the ground state $|g\rangle = |5^2S_{1/2}, F = 1, m_F = 0\rangle$. The atoms remaining in the $|5^2S_{1/2}, F = 2\rangle$ manifold are pushed out of the measurement zone by applying a circularly polarized laser beam that is resonant to the $|5^2S_{1/2}, F = 2\rangle \rightarrow |5^2P_{3/2}, F = 3\rangle$ transition. The two so-called clock states $|g\rangle$ and $|e\rangle$ are chosen as they are sensitive to magnetic fields only to the second order, which strongly reduces the impact of external magnetic fields onto the internal level shift, and thereby on the interferometer phase and signal contrast. In order to discriminate between the Zeeman sublevels and to only address the $m_F = 0$ states, a homogeneous magnetic bias field is applied in the interferometer region (see Fig. 2a). This allows to address a pair of entangled states, which are in our case:

$$|g\rangle \otimes |p = 0\rangle = |g, 0\rangle \tag{9}$$

$$|e\rangle \otimes |p = \hbar k_{\text{eff}}\rangle = |e, \hbar k_{\text{eff}}\rangle \tag{10}$$

with p being the atomic momentum in the beam-splitting direction.

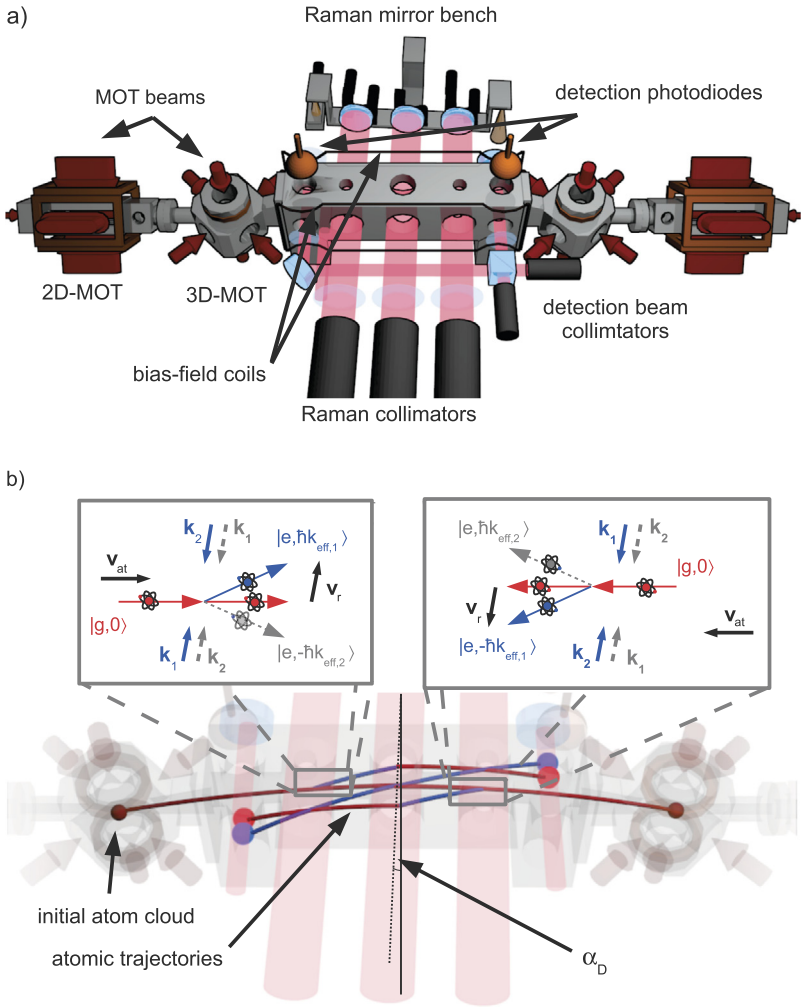

Fig. 2. (Colour online.) Gyroscope apparatus. (a) The gyroscope apparatus is depicted here including light fields, optics, vacuum chamber, and copper coils for magnetic field generation. (b) The atom interferometer trajectories are depicted in red and blue for atomic paths on which the atoms are in ground and excited state, respectively. The common angle of the Raman light fields with respect to the atomic forward velocity direction is slightly differing from 90° by the Doppler angle α_D, which allows the selection of either of the two beam-splitting directions $\mathbf{k}_{\mathrm{eff},1}$ and $\mathbf{k}_{\mathrm{eff},2}$ via the relative Raman laser detuning (see text). The atom interferometer is depicted here for the case $\mathbf{k}_{\mathrm{eff},1}$ in colour, and for $\mathbf{k}_{\mathrm{eff},2}$ in grey dashed representation.

3.2. Raman light fields

Raman beam-splitting is enabled through three pairs of spatially separated light fields generated by two power-amplified external cavity diode lasers (ECDL). As the relative phase of these two lasers is transferred to the interferometer states, it is required to be highly stable within the duration of each interferometer sequence. This is realized by stabilizing the beat of the two lasers onto an ultra-stable low-noise microwave reference at about 6.834 GHz, similar to the work presented in [22]. The laser light emitted by both lasers is superimposed and guided to the experimental setup in three polarization-maintaining single-mode fibres. Their output is collimated each to a beam of 19 mm waist, resulting in a triplet of parallel, horizontal beams (see Fig. 2) with centre separations of 65 mm.

The three Raman beams are retro-reflected on single mirrors that form two pairs of counter-propagating light fields in each beam. All three mirrors are mounted on a common aluminium support structure. The two outer mirrors are remotely controllable in horizontal and vertical tilt using piezo stepper motors. Also the whole support structure itself can be controlled in both tilt directions using pairs of piezo stepper motors and piezo stacks for coarse (stepwise) and fine (continuous) adjustment, respectively. The Raman retro-reflection mirrors feature a common angle α_D with respect to the forward velocity of the atomic trajectories (see Fig. 2b). This adds a frequency shift $\pm\omega_D = \pm v_x k_{\mathrm{eff}} \sin(\alpha_D)$ to the Raman transition arising from the two-photon transition Doppler shift for horizontal atomic velocity v_x. In the presence of all four light fields in our retro-reflected setup, this results in two resonances in each direction for frequencies $+\omega_D$ and $-\omega_D$, which correspond to momentum transfers $\mathbf{k}_{\mathrm{eff},1}$ and $\mathbf{k}_{\mathrm{eff},2} = -\mathbf{k}_{\mathrm{eff},1}$. Each of the resonances can be addressed by adding

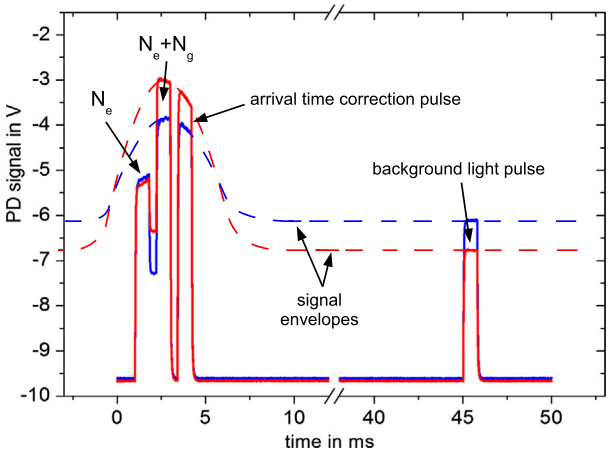

Fig. 3. (Colour online.) Detection signal example. The photodiode signals allow us to deduce the amount of light scattered by the atomic clouds during the travel through the detection zone. The signal is depicted for the two interferometers in red and blue, respectively. The expected signal envelopes for continuously applied detection light is depicted as dashed line. The average height of the four pulses is recorded in order to compute the transition probability P_e for each interferometer (see text).

the Doppler frequency to the frequency difference of the two Raman lasers.[1] As the two interferometers feature opposed forward velocities, the interferometer with $\pm v_x$ is transferred a momentum $\pm\hbar\,\mathbf{k}_{\mathrm{eff},1}$ and $\mp\hbar\,\mathbf{k}_{\mathrm{eff},2}$ as depicted in Fig. 2b. Hence, the two interferometers feature opposite momentum transfer directions and the acceleration-induced phase shifts carry opposite signs in the two interferometers, whereas the phase shift induced by rotations is common for both. This is used for distinguishing accelerational and rotational phase shifts as initially introduced in Section 2.

Whereas acceleration-induced phase shifts can be discriminated from those induced by rotations by the use of two interferometers, phase shifts arising from the influence of electromagnetic fields to the internal atomic structure, such as differential AC-Stark shifts and quadratic Zeeman shifts, are also imprinted onto the rotation phase. However, in case they do not comprise a gradient along the direction of the atomic beam-splitting $\hat{\mathbf{k}}_{\mathrm{eff}}$, these shifts can be discriminated from rotation phase shifts by employing the so-called k-reversal technique. This consists in alternating the beam-splitting direction in subsequent measurement cycles and computing the interferometer phase pairwise from subsequent measurements employing $\mathbf{k}_{\mathrm{eff},1}$ and $\mathbf{k}_{\mathrm{eff},2}$, respectively, which corresponds to simultaneously reversing the area of both interferometers [23]. The resulting alternation of the rotation signal allows to suppress the k-invariant parts of the phase shift Φ_{EM}, namely AC-Stark and Zeeman induced shifts, by performing the half-difference of subsequent measurement results.

3.3. Interferometer read out

The interferometer phase is imprinted on the populations of the two interferometer states $|g,0\rangle$ and $|e,\hbar\,k_{\mathrm{eff}}\rangle$. These populations are determined in an internal-state-selective fluorescence detection subsequent to the last beam-splitting pulse when the atom clouds pass through the pulsed detection beams, as depicted in Fig. 2. The internal state population is measured in a sequence of four pulses. During the first pulse a fluorescence signal N_e proportional to the excited state population is measured using circularly polarized laser light to drive a closed transition between the states $5^2S_{1/2}$, $F=2$ and $5^2P_{3/2}$, $F=3$. Between these pulses, a pulse with laser light resonant to the $5^2S_{1/2}$, $F=1\rightarrow 5^2P_{3/2}$, $F=2$ transition optically pumps all atoms from the ground to the excited state. The third pulse probes once more the number of atoms in the excited state, which now results in the signal $N=N_g+N_e$ proportional to the total number of atoms. All light fields are set up in a retro-reflected configuration in order to prevent for pushing the atoms out of the detection zone during the pulse sequence. In order to suppress the electronic noise, the detection pulses require a minimal duration of 800 µs.

The fluorescence signal is given by a convolution of the atomic cloud size and of the detection beam shape. Together with the light-pulse sequence, this results in a profile depicted in Fig. 3. As the pulse application takes place at a fixed time in the measurement sequence, the detection signal shape depends on the arrival time of the atomic sample. In particular, N_e is reduced in case of a delayed arrival and rises if the atomic sample arrives early in the detection zone. The second pulse height however remains stable for small arrival time fluctuations as it corresponds to the maximum of the detection signal envelope. This introduced the purpose of the fourth pulse during which the total number of atoms is detected a second time, but on the flank opposite to N_e. The ratio of the signal height of this latter pulse to N allows us to deduce the arrival time variation, and therefore also to correct for this effect on N_e in the detection data treatment.

[1] Changing the relative Raman laser detuning also slightly modifies the absolute value of $\mathbf{k}_{\mathrm{eff}}$, and therefore of the interferometer scaling factor. However, this modification only adds a modification on the ppb level and is therefore negligible here.

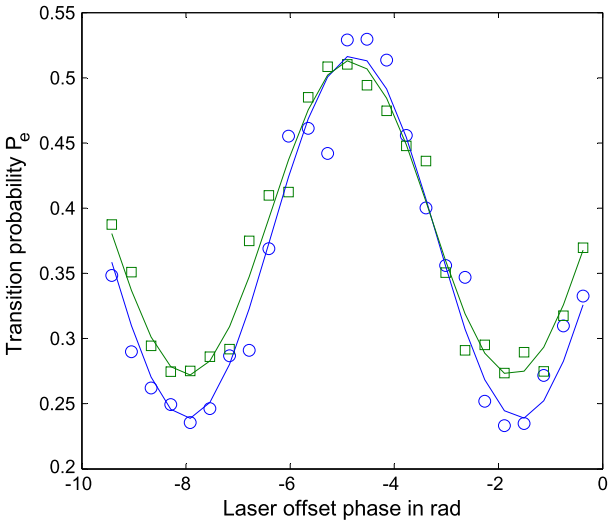

Fig. 4. (Colour online.) Interferometer signals. The measured interferometer signals are given by the transition probability P_e depicted as symbols here for interferometers 1 (blue) and 2 (green) with the corresponding fitted sinusoidal curves (lines).

A final pulse is applied after the atoms have left the detection zone in order to determine the background signal that is subtracted from each of the three pulse signals. Furthermore, the detection light intensity is monitored on the output of the detection light fibre in order to correct for intensity fluctuations. All this is then combined in a data treatment that results in a detection signal of the normalized excited state population corrected for errors arising from intensity jitter, background light fluctuations, and (small) arrival time fluctuations.

Since N_e is recorded on the side of the detection profile, the transition probability is not normalized when computing $P_e = N_e/(N_e + N_g)$. As our data treatment does not compensate for this effect, the absolute values of the normalized transition probability are slightly underestimated throughout the article. However, we only consider the signal noise in relation to the signal amplitude. The underestimation therefore has no impact on the noise and stability analyses.

3.4. Gyroscope test bench

The gyroscope apparatus is mounted on a test bench consisting of two MinusK 650BM-1 vibration isolation platforms that are connected using two H-shape steel beams. The breadboard carrying the apparatus rests on 14 Sorbothane® half-spheres in order to prevent vibrations induced by possible acoustic modes of the steel beams from being transferred to the atom interferometer setup. In order to avoid ambient magnetic fields to influence the interferometer measurement, and for reliable realization of the atomic launch, the apparatus is shielded by a mumetal enclosure.

4. Rotation sensitivity

Taking into account the atomic forward velocity, the free evolution time, and the effective wave vector of the beam-splitting process, we deduce a rotation-to-phase scaling factor of 4.7×10^4 rad per rad s^{-1} following Eq. (4). In order to deduce the gyroscope measurement performance, we first record interferometer characteristic curves $P_e(\Phi)$ by scanning the relative Raman laser phase of the third beam-splitting pulse. Fig. 4 shows typical fringes for both interferometers revealing fringe peak-to-valley values of at least 28% and 24%, respectively. A repeated transition probability measurement on mid-fringe then reveals a per-shot phase noise of 210 mrad and 225 mrad for the two interferometers, respectively, 213 mrad in the acceleration phase, and 47 mrad in the rotation phase. Taking into account the interferometer cycle time of 0.4 s, this corresponds to a residual noise in the range of 600 nrad s^{-1} Hz$^{-1/2}$ for our gyroscope in a 1-s measurement time. Depending on the exact environmental conditions in terms of vibrations, we observe sensitivities between 550 and 660 nrad s^{-1} Hz$^{-1/2}$ in our gyroscope.[2] From independent measurements, we infer that the short-term sensitivity is limited partially by the noise of the detection process (of the order of a few 10^{-3}), and partially by residual rotation vibrations of the platform.

[2] The level of vibrations of the laboratory floor depends on human activities in the our building, which is the reason for the short term sensitivity values to vary throughout this article.

5. Stable gyroscope operation

Whereas the influence of accelerations onto the rotation phase is highly suppressed, it can have a deleterious effect on the read out of the rotation signal in case the acceleration phase causes the signal to leave the so-called mid-fringe position, and to scan over many fringes resulting in ambiguities in the phase read out. This is induced by seismic noise inducing vibrations of the apparatus, and also by varying platform orientations resulting in fluctuations in the projection $\mathbf{k}_{\text{eff}} \cdot \mathbf{g}$. We have implemented two methods that mitigate for these effects.

The first method relies on a closed-loop stabilization of one of the two interferometers to mid-fringe operation by acting on the vertical Raman retro-reflection mirror orientation. This results in changing the effective wave vector projection onto gravity and hence the acceleration phase. By realizing the stabilization for one interferometer, the acceleration phase of the second interferometer is automatically stabilized as the mirror orientation is common to both interferometers with opposite sign since the transferred momenta have opposite sign. The rotation phase can be read out simply by performing the phase sum as before. This technique, which allows the mitigation of slowly fluctuating acceleration phase shifts, will be discussed in Section 5.1.

The second technique is based on an approach complementary to the first. It directly exploits the correlation of the two interferometers in the presence of large acceleration phase variations using an ellipse fitting method for the extraction of the rotation signal. This method is described in [24] for the signal read out in an atomic gravity gradiometer. Although is comes with a slight decrease in sensitivity, this technique holds essential advantages for our present setup as it allows us to suppress transition probability offset drifts of the interferometer fringe signal if these are slow versus the interferometer's cycle time. Furthermore, this technique is particularly interesting for future applications in environments showing higher vibration levels, as well as for atom gyroscopes with larger areas.[3] It will also enable reliable phase read out when scaling up the interferometer area, which would also increase the acceleration phases arising from platform tilting and vibrations. We implement this method by modulating the acceleration phase via the Raman mirror orientation, which is reported in Section 5.2.

5.1. Mid-fringe lock

A prior determination of the fringe parameters from data such as those depicted in Fig. 4 allows one to derive an error signal from the mid-fringe measurement. This error signal is deduced from the interferometer phase, which can be determined via the transition probability P_{e} on an interval of $[0, \pi)$ using

$$P_{\text{e},i} = P_{0,i} + A_i \cdot \cos(\Phi_i) \tag{11}$$

$$\Rightarrow \quad \Phi_i = \cos^{-1}\left(\frac{P_{\text{e},i} - P_{0,i}}{A_i}\right) \tag{12}$$

where $P_{0,i}$ and A_i are offset and amplitude of the interferometer fringe of the interferometer i with $i = 1, 2$. It is then digitally processed in order to be fed back to the piezo stepper motor that vertically tilts the common mount of the three Raman laser retro-reflection mirrors. The projection of the wave vector onto gravity is thereby employed to correct for slow drifts of the acceleration phase.

Figs. 5 and 6 show the interferometer running for 500 shots respectively with open and closed fringe stabilization feedback loop. The effect of the fringe lock becomes clearly visible here: whereas without the fringe lock, the acceleration phase variation induces both interferometers to leave one fringe, it remains in mid-fringe position in the case of the closed loop. In fact, no proper phase calculation is possible in case the interferometer phase is close to $n\pi$ ($n \in \mathbb{Z}$), corresponding to top and bottom fringe positions. However, locking the interferometer signal to mid-fringe allows the stable interferometer phase to be read out over a long time. The short-term performance of the gyroscope reaches similar values as before. The short-term sensitivity in the locked case is found to be as low as 660 nrad s^{-1} $\text{Hz}^{-1/2}$. Consequently, the stepwise corrected mirror orientation does not induce detrimental rotational vibration modes in the mirror mount of the platform. Whereas this technique has been employed here for signal stabilization, it can more generally be used to keep the interferometer orientation horizontally stable throughout the whole measurement.

5.2. Correlated phase modulation

The modulation-based stable interferometer readout scheme relies on the strict anti-correlation of the acceleration phases. Whereas this technique is particularly well-suited for application in environments with strong acceleration-induced phase noise in the range of π and above, this noise is much smaller in our case. We therefore induce a modulation of the vertical beam splitter mirror orientation using the vertical piezo stack (and thus of the $\mathbf{k}_{\text{eff}}$ orientation) in order to commonly modulate the acceleration phase of both interferometers. An acceleration phase shift of $\Delta\Phi_{\text{a}} = 2\pi$ is found for

[3] When increasing the interferometer area in order to increase the gyroscope sensitivity, also the susceptibility to acceleration increases, leading to a smaller required modulation of the wave vector projection to $\mathbf{g}$.

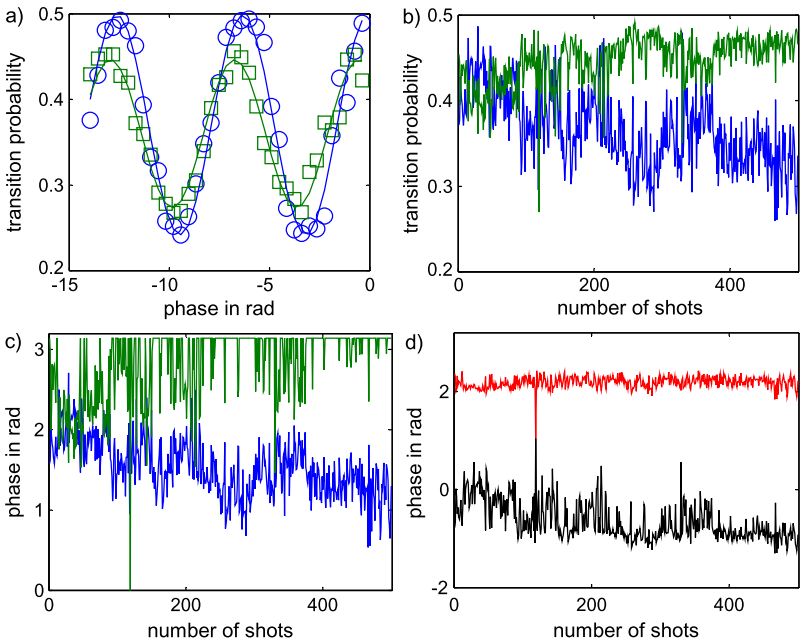

Fig. 5. (Colour online.) Fringe lock switched off. (a) Interferometer signals (symbols, blue: interferometer 1, green: interferometer 2) and corresponding fits for a Raman laser phase scan (lines). (b) Interferometer signals in a repeated measurement of 500 shots length, (c) inferred interferometer phases, (d) derived rotation (red) and acceleration-like phase (black).

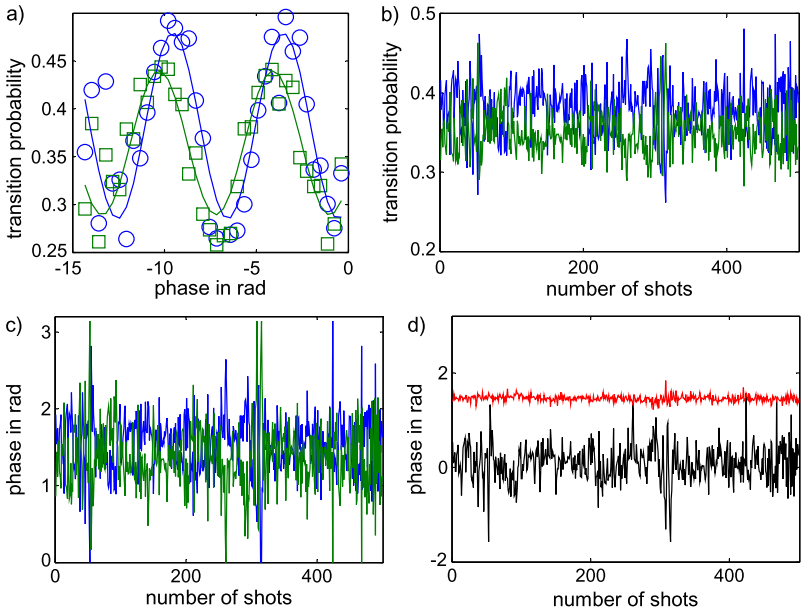

Fig. 6. (Colour online.) Fringe lock switched on. (a) Interferometer signals (symbols, blue: interferometer 1, *green:* interferometer 2) and corresponding fits for a Raman laser phase scan. (b) interferometer signals in a repeated measurement of 500 shots length, (c) inferred interferometer phases, (d) derived rotation (red) and acceleration-like phase (black).

an angle modulation of $\Delta\alpha = 75$ µrad using Eq. (6). Although this brings along a modulation of the atom interferometer area orientation, and therefore of the rotation phase, this influence is negligible for our experimental parameters. The latter can be seen as a variation of the projection $\mathbf{n}_A \cdot \boldsymbol{\Omega}_{\text{Earth}}$ with $\mathbf{n}_A = \mathbf{A}|\mathbf{A}|^{-1}$, which results in estimated fluctuations in the measured rotation rate and rotation phase values using Eq. (4) of only $\Delta(\mathbf{n}_A \cdot \boldsymbol{\Omega}_{\text{Earth}}) \approx 1$ nrad s^{-1}. Moreover, the rotation rate modulation is not limited to this value when scaling up the interferometer: If the interferometer area is enlarged by increasing the pulse separation time, the acceleration modulation also only requires smaller angles, leading to a smaller rotation rate modulation.

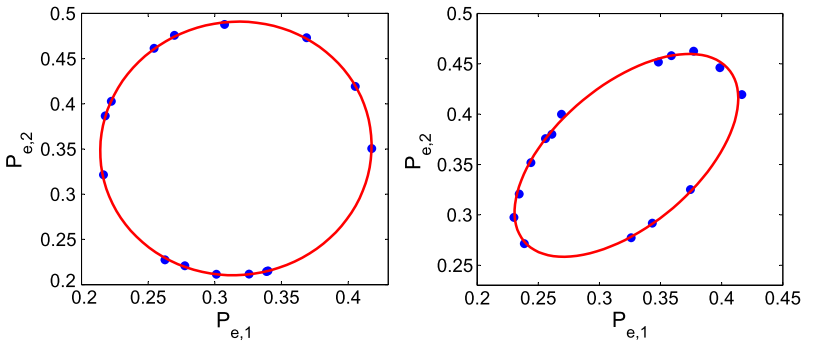

Fig. 7. (Colour online.) Ellipse fit examples. A set of 15 shots with results $(P_{e,1}, P_{e,2})$ (blue dots) is plotted parametrically and fitted by an ellipse (red line), which allows us to extract the common phase of the two correlated interferometers. The ellipses are shown for both beam splitter momentum transfer directions, $\mathbf{k}_1$ (left) and $\mathbf{k}_2$ (right).

The employed ellipse fit method (Fig. 7) follows the realization in [24] based on the parametric representation $(P_{e,1}, P_{e,2})$ of the two interferometers with

$$P_{e,1} = P_{0,1} + A_1 \cos(\Phi_1) \tag{13}$$

$$P_{e,2} = P_{0,2} + A_2 \cos(\Sigma\Phi - \Phi_1) \tag{14}$$

where $\Sigma\Phi = \Phi_1 + \Phi_2$. The rotation phase is determined from this plot by fitting the conic form

$$\mathbf{u} \cdot \mathbf{x} = Ax^2 + Bxy + Cy^2 + Dx + Ey + F = 0 \tag{15}$$

to the data set, where $\mathbf{x} = (x^2, xy, y^2, x, y, 1)$ and $\mathbf{u} = (A, B, C, D, E, F)^{\mathrm{T}}$. Fitting is realized using a least-squares (LSQ) fit method yielding the parameter values of the conic representation. From this, we can extract the common phase of the two interferometers, which reads as:

$$\Sigma\Phi = \cos^{-1}\left(\frac{-B}{2\sqrt{AC}}\right) \tag{16}$$

As introduced in Section 2, the acceleration-induced phase shifts in the two interferometers have respectively opposite signs. The ellipse fit method therefore yields the phases that contribute with the same sign to the phases of both interferometers, and by using Eq. (5) we find:

$$\frac{\Sigma\Phi}{2} = \Phi_\Omega + \Phi_{\mathrm{laser}} + \frac{\Phi_{\mathrm{EM},1} + \Phi_{\mathrm{EM},2}}{2} \tag{17}$$

$\Phi_{\mathrm{EM},1}$ and $\Phi_{\mathrm{EM},2}$ are then rejected in the k-reversal technique introduced in Section 3.2. Tuning the relative Raman laser phase Φ_{laser} along the interferometer sequence allows us to choose the opening of the ellipse. This leaves us with the rotation-induced phase shift Φ_Ω plus possible systematic phase shifts.

The number of points for each fit is chosen by a trade-off of gyroscope spectral resolution and fit uncertainty. A certain number of points is needed to be able to identify the ellipse shape in a fit. Furthermore, the modulation frequency should not be too high in order to minimize vibrations of the platform. We find a number of 15 points for each fit for an effective repetition rate of about 1 Hz in the k-reversal measurement, and a modulation frequency of 100 mHz to optimally meet these demands.

The rotation sensitivity is slightly reduced using the ellipse fit method compared to mid-fringe operation as not both interferometers are necessarily driven at the same optimal operation point. We chose the phases to be in quadrature by tuning the laser phase before the last beam-splitter pulse in order to get an open ellipse, which yields best fit results. Taking into account the typical normalized detection noise in the order of 10^{-3}, a numerical estimation results in a typical excess factor in short-term noise of approximately 1.5. This is confirmed by our measurements in which we observe a typical short-term sensitivity of 850 $\mathrm{nrad\,s^{-1}\,Hz^{-1/2}}$ (compared to 550 $\mathrm{nrad\,s^{-1}\,Hz^{-1/2}}$ in the case of a free-running mid-fringe measurement performed before the integration measurement).

On the one hand, this technique shows slightly higher readout noise. On the other hand, it is perfectly suited for usage in the environment of a vibration noise that induces a phase noise exceeding π, where all other commonly used phase-read-out techniques fail. We choose this read-out technique for the analyses presented in Section 6 as it additionally mitigates interferometer fringe offset fluctuations, which are observed to induce spurious rotation signals in the case of the fringe-lock technique.

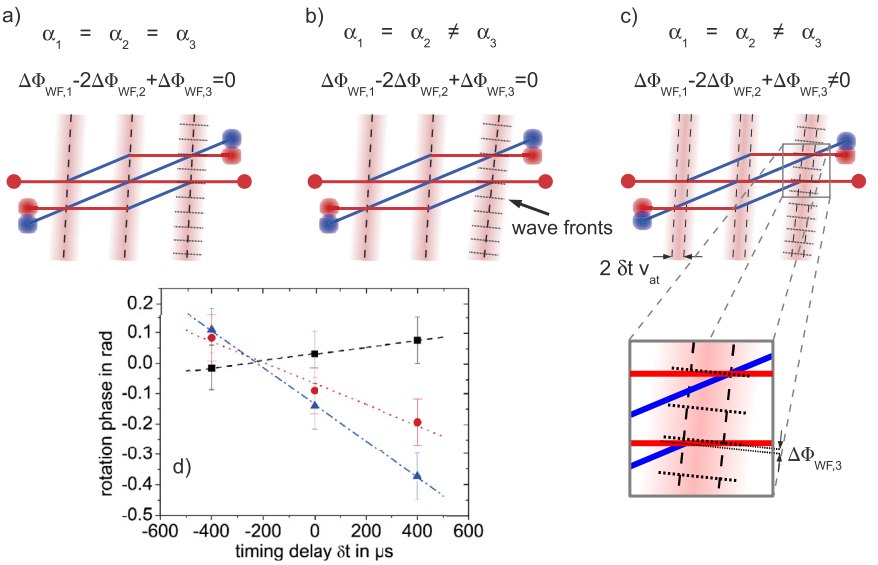

Fig. 8. (Colour online.) Induced pulse application mismatch. The atomic trajectories and the three interaction zones are shown in top view for optimal timing and optimal alignment (a), optimal timing with imperfect alignment (b), and for a timing delay δt before the application of the Mach–Zehnder sequence with imperfect alignment (c), respectively. (d) The graph depicts rotation phase values as a function of the induced cloud overlap mismatch for three different horizontal tilt angles of one of the outer Raman mirrors. The error bars take into account the phase error between subsequent measurements due to slow fluctuations. The statistical uncertainty on each point is below 20 mrad. A wave-front induced phase $\Delta\Phi_{\mathrm{WF},i}$ with $i = 1, 2, 3$, can be derived for each pulse leading to a total wave front phase, which is observed as a phase variation as shown in (d). The sketches are not to scale.

6. Impact of the use of three pairs of Raman beams

Using three Raman retro-reflection mirrors holds the advantage of scaling up the interferometer size, but it implies high demands of the relative beam alignment. As the two light fields needed for driving the Raman process are guided to the experiment on a common path, the beam shape and wave fronts (thus including the wave front tilt) are identical for both beams at the position of the atoms. However, one of the two light fields is reflected before interacting with the atoms, which is why the spatial part of the phase transferred to the atoms during atom–light interaction in the Raman process is defined by the retro-reflection setup (vacuum chamber windows and retro-reflection mirror). In particular, the mirror orientation (together with the wedges of the chamber windows) defines the effective wave front tilt of each pair of Raman beams. The total interferometer phase (5) therefore comprises a phase that corresponds to the sum of the normal mirror–atom distances in each shot. Hence, in case of a relative tilt of the three Raman beams, the single pulse phases can be different for atoms that interact with the Raman light fields at different positions. If this dephasing is as large as 2π across the atomic cloud diameter, the integrated interferometer contrast vanishes as the transition probability is recorded for all atoms at once without spatial resolution in the fluorescence detection. This sets strong requirements on the relative tilt alignment of the retro-reflection mirrors, which is found to be in the range of 10–20 μrad. We therefore implemented an alignment procedure involving the interferometer signal contrast in different interferometer configurations to align the three Raman beam retro-reflection mirrors, which is described in detail in [25].

Not only the fringe contrast, but also the interferometer phase offsets are influenced by residual relative tilts of the Raman retro-reflection mirrors. This phase shift carries opposite signs for the two interferometers and is therefore suppressed similar to accelerations. However, in case the interferometers do not overlap, a rotation bias occurs (see Fig. 8). This can be observed as a bias on the half-sum of the two interferometer phases and therefore on the measured rotation rate as we deliberately induce an interferometer overlap mismatch. We realize this by adding a variable offset δt to the pulse timing, which changes the distance of the atomic samples of the two interferometers during beam-splitting pulse application. The rotation phase bias is plotted versus the timing mismatch in Fig. 8 for different tilt angles of one of the outer Raman retro-reflection mirrors.

As source position fluctuations are correlated in the vertical and anti-correlated in the horizontal direction in our setup, it is sufficient to consider the latter. In case of a horizontal position fluctuation Δx, the overlap of the two interferometers deviates by $2\Delta x$. The fixed experimental cycle causes the atomic arrival time in our detection scheme to vary as a function of the position of the source. We can therefore use the arrival time as a measure of the position, which we confirm by measuring the latter using a CCD (charged-coupled device) camera taking a picture of the atom clouds before launch.

Measuring the source position fluctuations allows us to deduce fluctuations of the atom interferometer overlap from the arrival time signals. The scaling from the arrival time to source position fluctuation and finally to rotation phase fluctuations mainly depends on the exact shape of the detection signal and on the respective Raman mirror tilt. A corresponding set of factors is found directly by correlation to the measured rotation signal. Fitting a linear combination of the arrival time

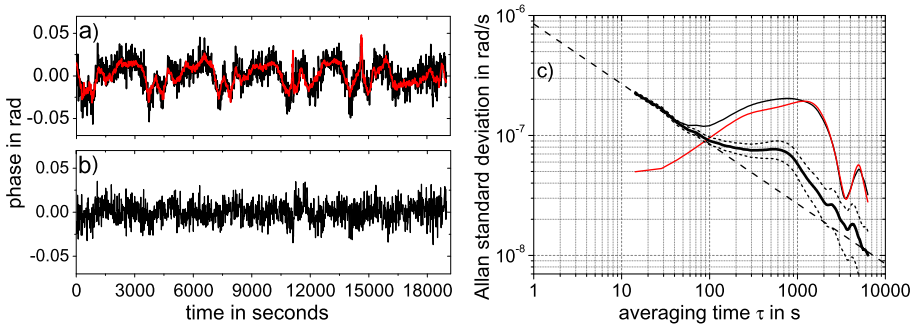

Fig. 9. Rotation rate averaging measurement. (a) The rotation phase (black) is plotted with the time series of expected rotation phase values deduced from the arrival time measurements (red). The coefficients for the latter are found in a fit of a linear combination of the atomic arrival times to the rotation signal. (b) Subtracting the expected phase values results in a suppression of the wave front influence on the rotation phase. Offsets have been removed. (c) The Allan standard deviation of the rotation signals corresponding to the rotation phases on the left side allows us to analyse the gyroscope stability. The dotted line represents the statistical errors of the Allan standard deviation, and the dashed line represents a $\tau^{-1/2}$ averaging at 850 nrad s^{-1} Hz$^{-1/2}$.

signals to the rotation phase therefore allows us to deduce the spurious rotation phase induced by fluctuating interferometer overlap coupled to residual effective wave front tilts of the Raman light fields. The rotation signal and the fitted linear combination of the arrival time signals are plotted in Fig. 9.

From the correlation, we can furthermore correct for this influence by subtracting the fitted curve from the rotation phase. This strongly improves the averaging behaviour of our gyroscope. Removing the slow signal oscillations allows us to average to a sensitivity to rotations of 20 nrad s^{-1} after 4000 s of integration, which is inferred from the Allan standard deviation also depicted in Fig. 9.

7. Conclusions

We have presented recent progress in rendering our atom gyroscope more stable against both, short and long term acceleration noise, i.e. vibrations and slow platform tilting, respectively. We have employed two different techniques for achieving this goal. The first one is based on an active feedback loop stabilizing the interferometer signal to the mid-fringe position from shot to shot through the control of the orientation of the atom interferometer. It results in a short term sensitivity of 660 nrad s^{-1} Hz$^{-1/2}$. The second stable read out method relies on an ellipse fit of the parametric representation of the two atom interferometer signals. It strikes with simplicity and high immunity against vibrations of the apparatus, which is important when running the gyroscope in noisy environments. Adding a modulation to the gyroscope orientation allows exploiting the interferometer's sensitivity to accelerations in order to achieve the desired correlated phase modulation required for ellipse fitting. This yields a highly robust read-out method that is immune not only against (non-rotational) vibrations acting on the device, but also against slow fluctuations in the interferometer's signal offset and amplitude in the device itself. We achieve a short-term sensitivity of 850 nrad s^{-1} Hz$^{-1/2}$ and enable studies on slowly changing spurious rotation signals by enabling robust long-term measurements. This technique is of particular interest not only for environments in which vibrations induce acceleration noise of multiples of 2π, but also for enabling technically more simple atomic gyroscopes, e.g., in cases where the normalization in the detection process is not stable over long times.

Using the ellipse-fit-based phase read out allowed us to identify the major source for long-term fluctuations of the device itself, a coupled effect of residual Raman beam misalignments and atom source position fluctuations. Furthermore, we have implemented a technique that allows us to correlate the observed spurious rotation rate with the atomic sample arrival time, and hence to correct the rotation signal for this influence. In integration of the rotation signal, we reach a resolution for rotations of down to 20 nrad s^{-1} after 4000 s of measurement time.

Whereas a detailed study of the instrument noise will be subjected to additional work, we can clearly derive from the work presented here that both the atom source position stability and the relative Raman beam alignment are crucial for a stable rotation measurement. The phase shift arising from the cross-coupling of source position and wave front quality should be suppressed by increasing the rotation-to-phase interferometer scaling factor. In the prospect of an improvement of our sensor or the development of new atom interferometer gyroscopes, this can be achieved by augmenting the free evolution time T. Techniques for enlarging the momentum recoil as double-diffraction technique [26], large-momentum transfer (LMT) beam splitters [27], or sequential beam-splitter pulses similar to the ones presented in [28] for the Bragg case have been proposed and demonstrated for enhancing interferometry scaling factors. Nevertheless, the wave-front induced phase shift is always proportional to the recoil momentum transferred to the atoms in the interferometer and scales up likewise. In contrast to this, an increase in T allows us to effectively suppress position-related phase shifts, which remain constant and are therefore suppressed quadratically when increasing T. Augmenting the free evolution time between two pulses requires either to realize smaller forward velocities, e.g., in spaceborne gyroscopes for measurements of the Lense–Thirring effect such as proposed in [29], or to increase the separation of the single mirrors. The latter necessitates a very good control

on the relative mirror alignment on large setups below the μrad regime.[4] Not only the relative mirror tilt and wave-front quality, but also the source position has to be well controlled. In this respect, it will be advantageous to replace molasses-cooled atomic ensembles of several μK temperatures with ultra-cold atoms with temperatures of nK in the next generation of a gyroscope. Recent progress in atom–chip based sources [30] make these highly promising candidates for sources used in atom interferometry with ultra-cold or even Bose–Einstein condensed matter when combined with launching techniques based on accelerated optical lattices [31].

The study of robust read out techniques performed in this paper will be of particular interest for gyroscopes that are envisaged for, e.g., navigational applications, such the gyroscope recently presented in [32], reaching repetition rates of 100 Hz. The modulation technique presented in our work could also be implemented in such interferometers of high repetition rate, both for modulation of the rotation and acceleration part, when choosing an appropriate mirror mounting in order to distinguish between both moments of inertia. Studies made here on the wave-front-induced phase shifts in the interferometer will also have to be considered in different atom interferometers. In particular when expanding the interferometer baseline and when employing technically demanding concepts as presented in [33] for the case of a space-borne gravity gradiometer, the cross-coupling between atomic trajectories and wave-front imperfections have to be taken into account, especially when striving for highest stabilities.

Acknowledgements

We would like to thank P. Bouyer for providing two Minus-K vibration isolation platforms that strongly helped us to realize the presented work. The research work for this article was supported in part by the Deutsche Forschungsgemeinschaft (SFB407), the European Union (Contr. No. 012986-2 (NEST), FINAQS, Euroquasar, IQS), and the Centre for Quantum Engineering and Space Time Research QUEST. G.T. acknowledges the support by the Max-Planck-Gesellschaft, the INTERCAN network, and the UFA-DFH.

References

[1] M.G. Sagnac, Sur la preuve de la réalité de l'éther lumineux par l'expérience de l'interférographe tournant, C. R. Acad. Sci. Paris 157 (1913) 1410–1413.
[2] W.W. Chow, J. Gea-Banacloche, L.M. Pedrotti, V.E. Sanders, W. Schleich, M.O. Scully, The ring laser gyro, Rev. Mod. Phys. 57 (1985) 61–104, http://dx.doi.org/10.1103/RevModPhys.57.61.
[3] G. Santarelli, P. Laurent, P. Lemonde, A. Clairon, A.G. Mann, S. Chang, A.N. Luiten, C. Salomon, Quantum projection noise in an atomic fountain: a high stability cesium frequency standard, Phys. Rev. Lett. 82 (1999) 4619–4622, http://dx.doi.org/10.1103/PhysRevLett.82.4619.
[4] R. Bouchendira, P. Cladé, S. Guellati-Khélifa, F. Nez, F. Biraben, New determination of the fine structure constant and test of the quantum electrodynamics, Phys. Rev. Lett. 106 (2011) 080801, http://dx.doi.org/10.1103/PhysRevLett.106.080801.
[5] H. Müller, S.-W. Chiow, Q. Long, C. Vo, S. Chu, A new photon recoil experiment: towards a determination of the fine structure constant, Appl. Phys. B 84 (4) (2006) 633–642, http://dx.doi.org/10.1007/s00340-006-2279-x.
[6] J.B. Fixler, G.T. Foster, J.M. McGuirk, M.A. Kasevich, Atom interferometer measurement of the Newtonian constant of gravity, Science 315 (5808) (2007) 74–77, http://dx.doi.org/10.1126/science.1135459, http://www.sciencemag.org/content/315/5808/74.full.pdf, http://www.sciencemag.org/content/315/5808/74.abstract.
[7] G. Rosi, F. Sorrentino, L. Cacciapuoti, M. Prevedelli, G.M. Tino, Precision measurement of the Newtonian gravitational constant using cold atoms, Nature 510 (2014) 518–521.
[8] J.P. Davis, F.A. Narducci, A proposal for a gradient magnetometer atom interferometer, J. Mod. Opt. 55 (2008) 3173.
[9] B. Canuel, F. Leduc, D. Holleville, A. Gauguet, J. Fils, A. Virdis, A. Clairon, N. Dimarcq, C.J. Bordé, A. Landragin, P. Bouyer, Six-axis inertial sensor using cold-atom interferometry, Phys. Rev. Lett. 97 (2006) 010402, http://dx.doi.org/10.1103/PhysRevLett.97.010402.
[10] T.L. Gustavson, P. Bouyer, M.A. Kasevich, Precision rotation measurements with an atom interferometer gyroscope, Phys. Rev. Lett. 78 (1997) 2046–2049, http://dx.doi.org/10.1103/PhysRevLett.78.2046.
[11] T.L. Gustavson, A. Landragin, M.A. Kasevich, Rotation sensing with a dual atom-interferometer Sagnac gyroscope, Class. Quantum Gravity 17 (12) (2000) 2385, http://stacks.iop.org/0264-9381/17/i=12/a=311.
[12] K.U. Schreiber, T. Klügel, J.-P.R. Wells, R.B. Hurst, A. Gebauer, How to detect the chandler and the annual wobble of the Earth with a large ring laser gyroscope, Phys. Rev. Lett. 107 (2011) 173904, http://dx.doi.org/10.1103/PhysRevLett.107.173904.
[13] A. Gauguet, B. Canuel, T. Lévèque, W. Chaibi, A. Landragin, Characterization and limits of a cold-atom Sagnac interferometer, Phys. Rev. A 80 (2009) 063604, http://dx.doi.org/10.1103/PhysRevA.80.063604.
[14] P.R. Berman (Ed.), Atom Interferometry, Academic Press, 1997.
[15] P. Meystre, Atom Optics, Springer, 2001.
[16] N.W. Ashcroft, N.D. Mermin, Solid State Physics, Harcourt College Publ., New York, 2000.
[17] C. Bordé, Atomic interferometry with internal state labelling, Phys. Lett. A 140 (1, 2) (1989) 10–12.
[18] C. Antoine, C.J. Bordé, Quantum theory of atomic clocks and gravito-inertial sensors: an update, J. Opt. B, Quantum Semiclass. Opt. 5 (2) (2003) S199, http://stacks.iop.org/1464-4266/5/i=2/a=380.
[19] T. Müller, M. Gilowski, M. Zaiser, P. Berg, C. Schubert, T. Wendrich, W. Ertmer, E.M. Rasel, A compact dual atom interferometer gyroscope based on laser-cooled rubidium, Eur. Phys. J. D (2009), http://dx.doi.org/10.1140/epjd/2009-00139-0.
[20] T. Müller, T. Wendrich, M. Gilowski, C. Jentsch, E.M. Rasel, W. Ertmer, Versatile compact atomic source for high-resolution dual atom interferometry, Phys. Rev. A 76 (6) (2007) 63611, http://www.citebase.org/abstract?id=oai:arXiv.org:0705.4544.
[21] M. Kasevich, D.S. Weiss, E. Riis, K. Moler, S. Kasapi, S. Chu, Atomic velocity selection using stimulated Raman transitions, Phys. Rev. Lett. 66 (1991) 2297–2300, http://dx.doi.org/10.1103/PhysRevLett.66.2297.
[22] G. Santarelli, A. Clairon, S. Lea, G. Tino, Heterodyne optical phase-locking of extended-cavity semiconductor lasers at 9 GHz, Opt. Commun. 104 (46) (1994) 339–344, http://dx.doi.org/10.1016/0030-4018(94)90567-3.

[4] Assuming an alignment uncertainty of 1 μrad, an interferometer phase shift of 8 mrad is induced per 1 mm interferometer overlap mismatch.

[23] D.S. Durfee, Y.K. Shaham, M.A. Kasevich, Long-term stability of an area-reversible atom-interferometer Sagnac gyroscope, Phys. Rev. Lett. 97 (2006) 240801, http://dx.doi.org/10.1103/PhysRevLett.97.240801.
[24] G.T. Foster, J.B. Fixler, J.M. McGuirk, M.A. Kasevich, Method of phase extraction between coupled atom interferometers using ellipse-specific fitting, Opt. Lett. 27 (11) (2002) 951–953, http://dx.doi.org/10.1364/OL.27.000951.
[25] G. Tackmann, P. Berg, C. Schubert, S. Abend, M. Gilowski, W. Ertmer, E.M. Rasel, Self-alignment of a compact large-area atomic Sagnac interferometer, New J. Phys. 14 (1) (2012) 015002, http://stacks.iop.org/1367-2630/14/i=1/a=015002.
[26] T. Lévèque, A. Gauguet, F. Michaud, F. Pereira Dos Santos, A. Landragin, Enhancing the area of a Raman atom interferometer using a versatile double-diffraction technique, Phys. Rev. Lett. 103 (2009) 080405.
[27] P. Cladé, S. Guellati-Khélifa, F. Nez, F. Biraben, Large momentum beam splitter using Bloch oscillations, Phys. Rev. Lett. 102 (2009) 240402, http://dx.doi.org/10.1103/PhysRevLett.102.240402.
[28] S.-w. Chiow, T. Kovachy, H.-C. Chien, M.A. Kasevich, 102ℏk large area atom interferometers, Phys. Rev. Lett. 107 (2011) 130403, http://dx.doi.org/10.1103/PhysRevLett.107.130403.
[29] C. Jentsch, T. Müller, E.M. Rasel, W. Ertmer, HYPER: a satellite mission in fundamental physics based on high precision atom interferometry, Gen. Relativ. Gravit. 36 (10) (2004) 2197–2221, http://dx.doi.org/10.1023/B:GERG.0000046179.26175.fa.
[30] H. Müntinga, H. Ahlers, M. Krutzik, A. Wenzlawski, et al., Interferometry with Bose–Einstein condensates in microgravity, Phys. Rev. Lett. 110 (2013) 093602, http://dx.doi.org/10.1103/PhysRevLett.110.093602.
[31] S.M. Dickerson, J.M. Hogan, A. Sugarbaker, D.M.S. Johnson, M.A. Kasevich, Multiaxis inertial sensing with long-time point source atom interferometry, Phys. Rev. Lett. 111 (2013) 083001, http://dx.doi.org/10.1103/PhysRevLett.111.083001.
[32] A.V. Rakholia, H.J. McGuinness, G.W. Biedermann, Dual-axis, high data-rate atom interferometer via cold ensemble exchange, arXiv:1407.3847v1.
[33] O. Carraz, C. Siemes, L. Massotti, R. Haagmans, P. Silvestrin, A spaceborne gravity gradiometer concept based on cold atom interferometers for measuring Earth's gravity field, arXiv:1406.0765v1.